ELSEVIER

Journal of Nuclear Materials 299 (2001) 91–100

journal of nuclear materials

www.elsevier.com/locate/jnucmat

Microstructure and properties of a Cu–Cr–Zr alloy

I.S. Batra *, G.K. Dey, U.D. Kulkarni, S. Banerjee

Materials Science Division, Bhabha Atomic Research Centre, Trombay, Mumbai 400 085, India

Received 2 May 2001; accepted 20 August 2001

Abstract

Copper-based dilute Cu–Cr–Zr alloys and their minor modifications, because of their excellent thermal conductivity, strength and fatigue resistance, are commonly used in an aged condition in heat transfer elements. However, in comparison to dilute Cu–Cr binary alloys in which the precipitation of chromium has been studied extensively in the last two decades, attempts at delineating the morphology, composition and crystallography of precipitates in Cu–Cr–Zr alloys have been few and only partially successful. The role of zirconium has also remained largely unresolved. In the present work, the precipitation in an alloy having a nominal composition of Cu–1 wt% Cr–0.1 wt% Zr has been shown to take place through the formation of a metastable ordered fcc phase. Also, the improvement in fatigue resistance due to the addition of zirconium has been ascribed to lowering of the stacking fault energy (SFE) of the alloy.

PACS: 28.52.Fa; 61.50.Ks; 81.30.Mh; 81.40.Cd

1. Introduction

Some copper alloys, well known for their high thermal conductivity, high strength and high fatigue resistance, are either being used or being considered for use for plasma facing components and divertor plates of Joint European Torus (JET), Next European Torus (NET), International Thermonuclear Experimental Reactor (ITER) and other similar fusion devices [1–3]. Cu–Cr–Zr alloy and some of its modifications are also being used [4–6] in certain other heat transfer elements. A heat transfer element is a thin walled structure with internal fins with cooling channels. Demineralised water, at high pressures ~1 MPa, is used as coolant in this. It works under high temperature gradients and for this reason, the alloy is expected to possess good thermal conductivity with a capacity to dissipate heat flux at a density of 15 MW m^{-2}. The alloy must also exhibit good mechanical properties including thermal fatigue resistance at 400 °C.

Cu–0.8 wt% Cr–0.08 wt% Zr alloy is used in the heat transfer element in an aged condition. The conventional aging treatment involves solution treatment of the alloy in vacuum/inert atmosphere at 980 °C for 45 min, quenching in water (or, preferably, in cold helium gas) followed by vacuum aging at 470 °C for 5 h. The material strength after the aging treatment depends upon the amount of chromium brought into supersaturation by the solutionising treatment. It is not possible to bring all the chromium into solution at 980 °C, as the solubility of chromium in copper at 1000 °C is only about 0.37 wt%.

Extensive literature is available on the microstructure [7–10], physical [11,12] and mechanical [13–15] properties, corrosion [16] and irradiation [17–19] behavior, and brazing [20] and joining [21] of the Cu–Cr–Zr alloy. These studies have been conducted mainly from the point of view of evaluating the alloy for its end use. Attempts [7–9] made to identify the nature, composition and distribution of precipitates in this alloy have been only partially successful. Precipitates with lobe–lobe contrast and precipitates with fringes parallel to the diffraction vector have been seen [7]. Tang et al. [8] have identified the precipitates in a slightly modified alloy to be Cu_4Zr and $CrCu_2(Zr, Mg)$. Surface oxide (Cu_2O)

* Corresponding author. Fax: +91-22 550 5151.
E-mail address: isbatra@apsara.barc.ernet.in (I.S. Batra).

0022-3115/01/$ - see front matter
PII: S0022-3115(01)00691-2

with Moiré-patterns has also been seen [7] using transmission electron microscopy (TEM). The role of zirconium in precipitation in Cu–Cr–Zr alloy as well as in improving the fatigue resistance of this alloy has remained largely unresolved. In contrast to this, binary Cu–Cr alloys have been well studied [22,23] from the precipitation point of view. The precipitates in dilute Cu–Cr alloys have been confirmed to be that of pure bcc chromium, irrespective of their sizes. The issue of their orientation relationship (OR) with the matrix has also been successfully resolved [23]. In the present work, an alloy with a nominal composition of Cu–1 wt% Cr–0.1 wt% Zr was studied using conventional transmission electron microscopy (CTEM) as well as high resolution transmission electron microscopy (HRTEM). From the results obtained, an attempt has been made to resolve the role of zirconium in precipitation and in improving the fatigue resistance of the alloy. In arriving at the conclusions, available [24,25] phase relationships in copper rich corner of the Cu–Cr–Zr alloy have been employed.

2. Experimental

To prepare the Cu–Cr–Zr alloy of the desired composition, small pieces of oxygen free high conductivity copper, electrolytic chromium and iodide zirconium, weighed in an appropriate ratio, were melted together in an induction furnace in a yittria lined graphite crucible. High purity argon was used as a protective atmosphere in the induction unit. The ingot weighing approximately 500 g was cut and cold rolled to a thickness of 0.4 mm. The strip thus obtained was cleaned and cut into small pieces of desired sizes.

Some small clean pieces were encapsulated in a quartz tube in helium, solutionised at 1000 °C for 1 h and then water quenched. At the time of the quench, the capsule was broken to obtain the fastest possible quench rate. Using these pieces, the peak aging temperature of this alloy was determined by measuring resistivity as a function of temperature in a highly sensitive automated four-probe resistivity set-up. For making these measurements, copper wires were spot welded onto the samples and used as current and potential leads. Heating and cooling of the samples was carried out at an extremely slow rate to ensure equilibrium during measurements.

To determine tensile properties, samples of 12.5 mm gauge length were machined out of the as rolled 0.4 mm thick strips, cleaned, encapsulated in quartz in helium, solutionised at 1000 °C for 1 h and then water quenched by breaking the capsule. These samples were again encapsulated in helium, aged at 480 °C for 5 h and then water quenched. These were tensile tested at a strain rate of 6.6×10^{-4} s^{-1} at room temperature and at 450 °C. For testing at each of these temperatures, at least three samples were employed.

For revealing the microstructure of the alloy in cold worked, solutionised and aged conditions, pieces, in the respective conditions, were metallographically polished to 1 μm diamond finish and then etched electrolytically in concentrated phosphoric acid.

For carrying out TEM, a small piece of the 0.4 mm thick strip was further rolled to 0.2 mm thickness and then chemically thinned to 0.1 mm thickness in a solution of 5% HF, 45% HNO_3 and 50% distilled water. Small pieces from this strip were encapsulated, and then solutionised and aged in the same manner as described above for tensile samples. 3 mm diameter discs were punched out of these aged pieces, mechanically thinned to about 0.07 mm and then jet thinned at room temperature in a solution having a ratio of 75 g chromic oxide, 375 cc acetic acid and 20 cc distilled water. Voltage, during electrolytic polishing, was maintained at about 50 V. The thinning process was terminated with the help of a photocell. Prior to loading in TEM, the jet thinned discs were ion milled for about 10 min to remove the surface oxide in a Gatan Duomill. These foils were examined in a JEOL 2000 FX microscope operating at 200 kV. In order to gain an improved understanding of the structural details of the fine precipitates that occur in the initial stages of the aging process, HRTEM examinations were carried out using a JEOL-3010 microscope operating at 300 kV and having a point to point resolution of 0.21 nm.

3. Results

3.1. Electrical resistivity vs. temperature

Using the four-probe technique, resistivity of samples, solutionised at 1000 °C for 1 h and then water quenched, was measured as a function of temperature during heating from room temperature to 650 °C as well as during cooling back to room temperature. A highly sensitive and automated data collection set-up was employed to obtain the variation shown in Fig. 1. Extremely slow heating and cooling rates (around 2 °C/min) were employed to ensure measurements at practically constant temperatures. From the variation depicted in Fig. 1, it is seen that initially the resistivity increases with temperature, as expected. At around 420 °C, the resistivity starts to drop indicating the onset of decomposition of the supersaturated solid solution. At 480 °C, a minimum in resistivity is attained which agrees well with the value of 470 °C obtained by Holzwarth et al. [7] for Cu–0.75 wt% Cr–0.1 wt% Zr alloy. Beyond this point, resistivity starts increasing once more with increase in temperature, albeit rather

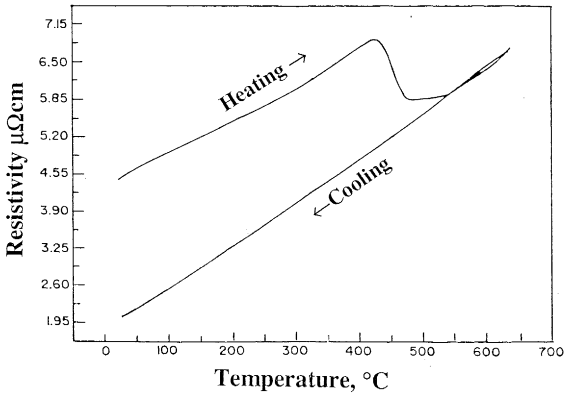

Fig. 1. Resistivity vs. temperature plot for solutionised and quenched Cu–Cr–Zr alloy.

slowly, until 550 °C – after which the rate of increase equals nearly the rate observed before the onset of decomposition. The slow variation between 480 and 550 °C indicates that all the processes involved in precipitation slowly come to an end. The low value of resistivity obtained at the room temperature after the thermal cycle indicates marked changes in the microstructure of the alloy due to precipitation. These changes have been examined in detail in the present work.

3.2. Tensile behaviour

True stress–true strain curves for the Cu–1 wt% Cr–0.1 wt% Zr alloy solutionised at 1000 °C for 1 h, water quenched and then aged at 480 °C for 5 h (referred to in this paper as the solutionised plus aged alloy) are depicted in Fig. 2. The yield strength, tensile strength and elongation, uniform as well as total, achieved in this alloy are compared with those of pure copper in Table 1. The significant gains due to the small additions of chromium and zirconium are obvious. The tensile properties achieved due to alloying and aging are in the desired range for the current as well as the envisaged end applications of the alloy.

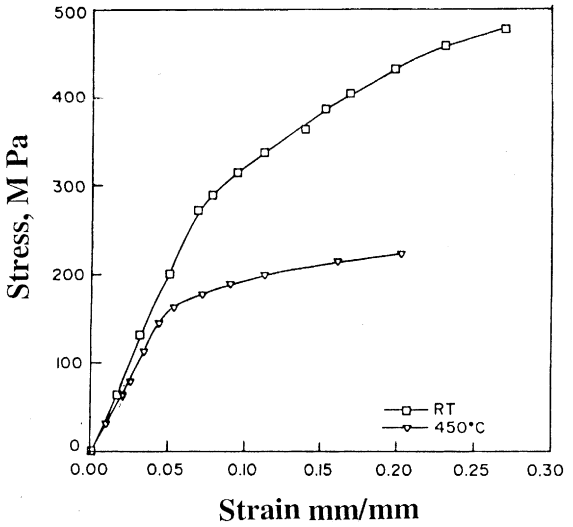

Fig. 2. True stress–true strain curves for the solutionised plus aged alloy at room temperature and 450 °C.

3.3. Microstructure

The microstructure of the solutionised plus aged alloy, as shown in the optical micrograph in Fig. 3, consisted of islands of eutectic regions in a matrix of copper. This microstructure was seen to resemble the microstructure of the simply solutionised alloy indicating that (i) all the precipitates formed during solidification of the alloy could not be dissolved by the solutionising treatment and (ii) the precipitates formed due to aging of the solutionised alloy at 480 °C for 5 h were submicroscopic. These submicroscopic precipitates are considered responsible for the enhanced strength due to aging. The need to identify these precipitates formed the basis of the use of the CTEM and the HRTEM to study this alloy.

Table 1
Tensile data

Material	Test temperature	Yield strength (MPa)	Tensile strength (MPa)	Uniform elongation[a] (%)	Total elongation[a] (%)
Pure copper (MARZ)[b]	RT	30–60	–	–	–
Pure copper (OFHC)[b]	RT	26	–	–	–
Cu–Cr–Zr alloy (solutionized)	RT	100	220	40	50
Cu–Cr–Zr alloy (aged)	RT	250	370	30	40
Cu–Cr–Zr alloy (aged)	450 °C	140	190	25	37

[a] Gauge length of the tensile samples was 12.5 mm.
[b] Ref. [1].

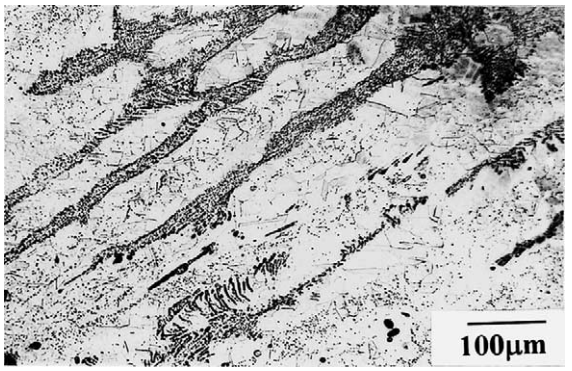

Fig. 3. Light micrograph of the solutionised plus aged alloy.

3.4. CTEM observations

3.4.1. Twinning

Fig. 4(a) shows the bright field (BF) micrograph depicting twins and the perpendicular portions (kinks) separating the twin facets. Fig. 4(b) is the corresponding selected area diffraction (SAD) pattern with [1 1 0] as the zone axis. The SAD pattern shown in Fig. 4(b) agrees with the commonly observed features of twinning seen in fcc alloy systems, namely, twinning (K_1) and first undistorted (K_2) planes being of type{1 1 1} and shear directions being of type $\langle 1\,1\,2\rangle$.

Also, twinning was found to be far more predominant in the alloy under investigation as compared to that generally seen in pure copper. This result indicates that addition of zirconium to a dilute copper–chromium alloy lowers its stacking fault energy (SFE), and it could also be the reason for the improved fatigue resistance of the ternary alloy. Lowering of SFE would lead to the dissociation of screw dislocations into their partials making cross-glide difficult and twinning rather easy and extensive. In other words, it means the alloy would be a planar-slip material in contrast to the wavy-slip nature of pure copper. This change in the nature of slip would eliminate [26,27] from the alloy the commonly observed tendency of formation of persistent slip bands (PSBs) during the fatigue failure of pure copper. Delay in the nucleation of fatigue cracks through the suppression of PSB formation because of the change in the nature of slip could thus be a plausible explanation for the reported [2,28] improved fatigue resistance of the Cu–Cr–Zr alloy.

Other microstructural features, which qualitatively corroborate the above hypothesis, were also observed in the CTEM images. A direct consequence of the lowering of the SFE by zirconium was the propensity for faulting observed in this alloy. Extended dislocation nodes (showing the typical 'Y' shape and marked in Fig. 5(a) by arrows) were seen at a number of locations in the sample. Fringe contrast arising from the planar faults was also observed. One such region is shown in the dark field (DF) image in Fig. 5(b).

3.4.2. Precipitation

Precipitation in alloys of similar composition has been shown previously [7] to have a bimodal distribution of precipitate sizes. The coarse precipitates are the ones that form during solidification of the alloy and do not dissolve completely during the solutionising treatment. The finer precipitates are the ones that form due to the decomposition of the supersaturated solid solution during aging.

One would expect to see large undissolved chromium-rich particles in the microstructure given that the chromium added to the original copper exceeded the solubility limit of approximately 0.37 wt% at the solutionising temperature of 1000 °C. Such large particles are actually a product of a eutectic reaction during solidification. A multitude of islands of such coarse

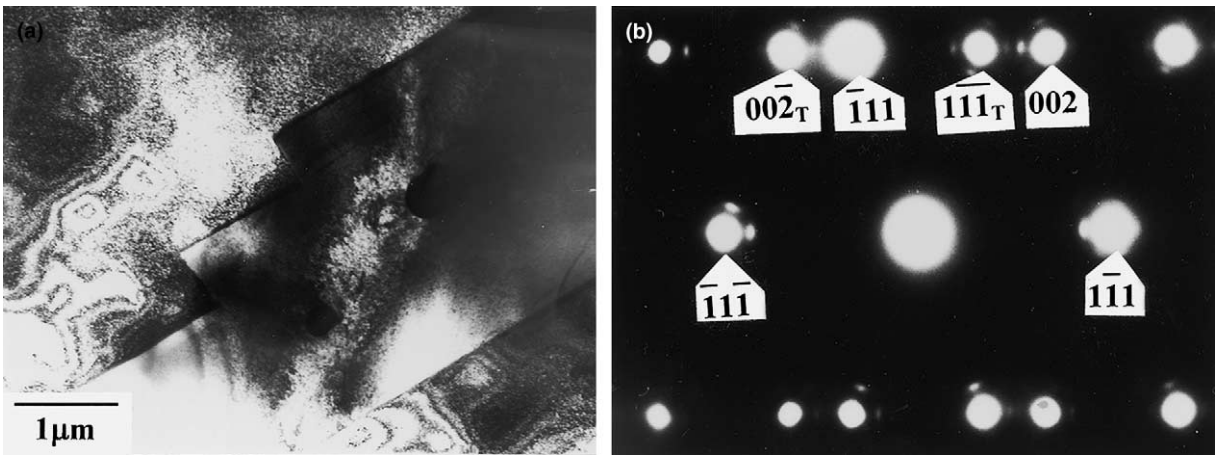

Fig. 4. (a) Bright-field micrograph of the solutionised plus aged alloy showing twins and (b) the relevant [1 1 0] SAD pattern.

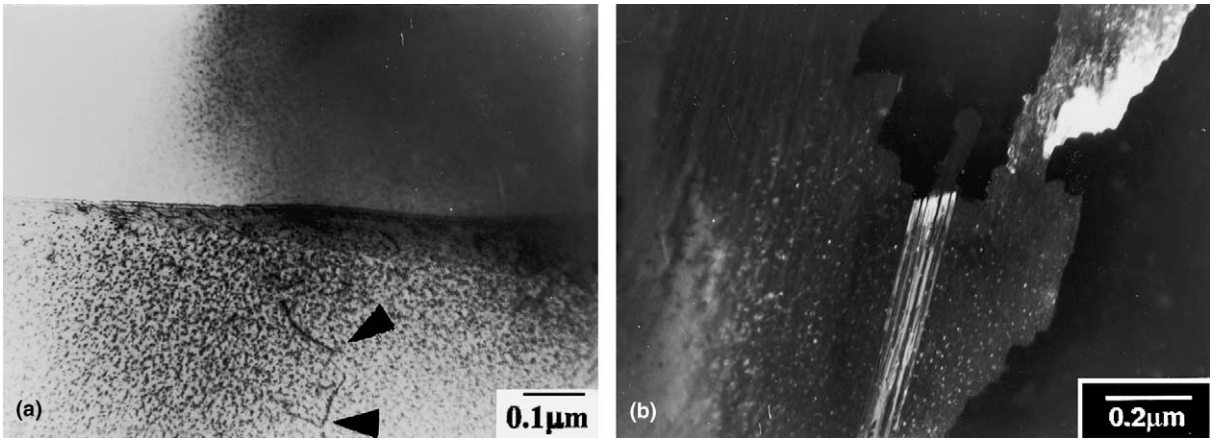

Fig. 5. (a) BF micrograph showing extended dislocations marked by arrows and (b) DF showing fringe contrast arising from a stacking fault in the solutionised plus aged alloy.

particles are shown in Fig. 3 in the previous section. The DF micrograph in Fig. 6(a) shows one such large particle (roughly 0.2 μm × 0.4 μm in size). The corresponding SAD, shown in Fig. 6(b) could be indexed to be [1 1 0] SAD of chromium.

In Fig. 7(a), SAD pattern with zone axis along $[1\,0\,0]_{fcc}$ is exhibited. It shows streaking in $\langle 1\,1\,0\rangle^*$ directions around the fcc reflections. This implies that, during the early stages of decomposition of the supersaturated solid solution, elastic strains are being generated along $\langle 1\,1\,0\rangle$ directions by the clustering of solute atoms. Tanner [29] has shown that a similar segregation of Be atoms on $\{1\,0\,0\}$ planes in Cu–2 wt% Be gives rise to elastic strains in $\langle 1\,1\,0\rangle$ directions. In the SAD depicted in Fig. 7(a), condensation of streaks into reflections of a second phase can also be seen. This indicates that precipitates of the second phase have already formed in some places of the region under examination. A faint superlattice reflection (marked by an arrow in the SAD) can also be seen midway between one of these reflections and the transmitted spot. This indicates that this phase, which appears to be a precursor to the formation of equilibrium bcc precipitates, is ordered.

Studies on dilute Cu–Cr alloys [22,23,30] and a quaternary Cu–Cr–Zr–Mg alloy [8] have established that, during the initial stages of precipitation, the bcc precipitates exhibit the well known Nishiyama–Wassermann (N–W) OR:

$$(1\,1\,1)_{fcc} \;//\; (1\,1\,0)_{bcc}$$

$$[0\,\bar{1}\,1]_{fcc} \;//\; [0\,0\,1]_{bcc}$$

$$[\bar{2}\,1\,1]_{fcc} \;//\; [\bar{1}\,1\,0]_{bcc}.$$

In this OR, the close-packed planes in the two phases, viz. $\{1\,1\,1\}_{fcc}$ and $\{1\,1\,0\}_{bcc}$ are parallel. However, a

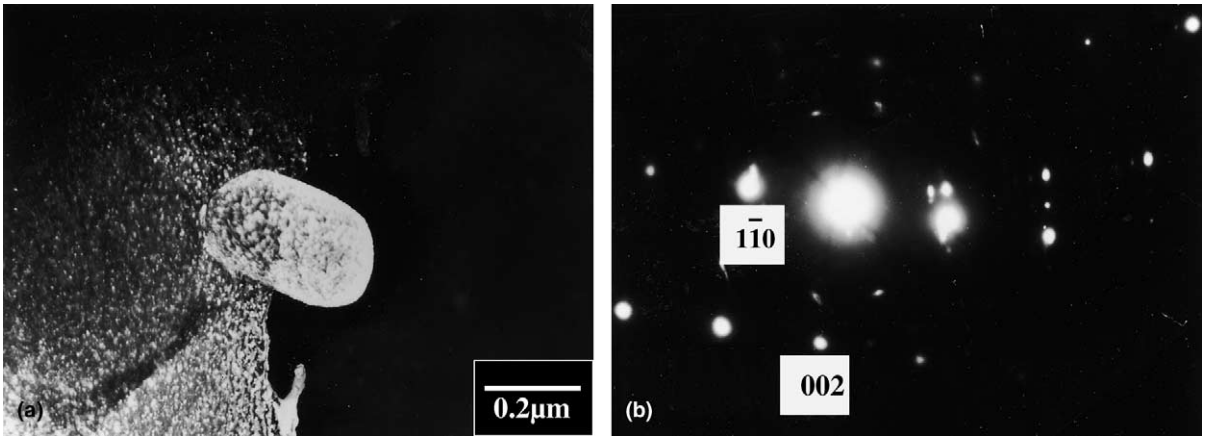

Fig. 6. (a) DF micrograph showing a large chromium particle and (b) $[1\,1\,0]_{bcc}$ SAD pattern from the particle. Presumably, this particle did not go into solution completely during solutinising since the chromium content of the alloy was in excess of the solubility limit.

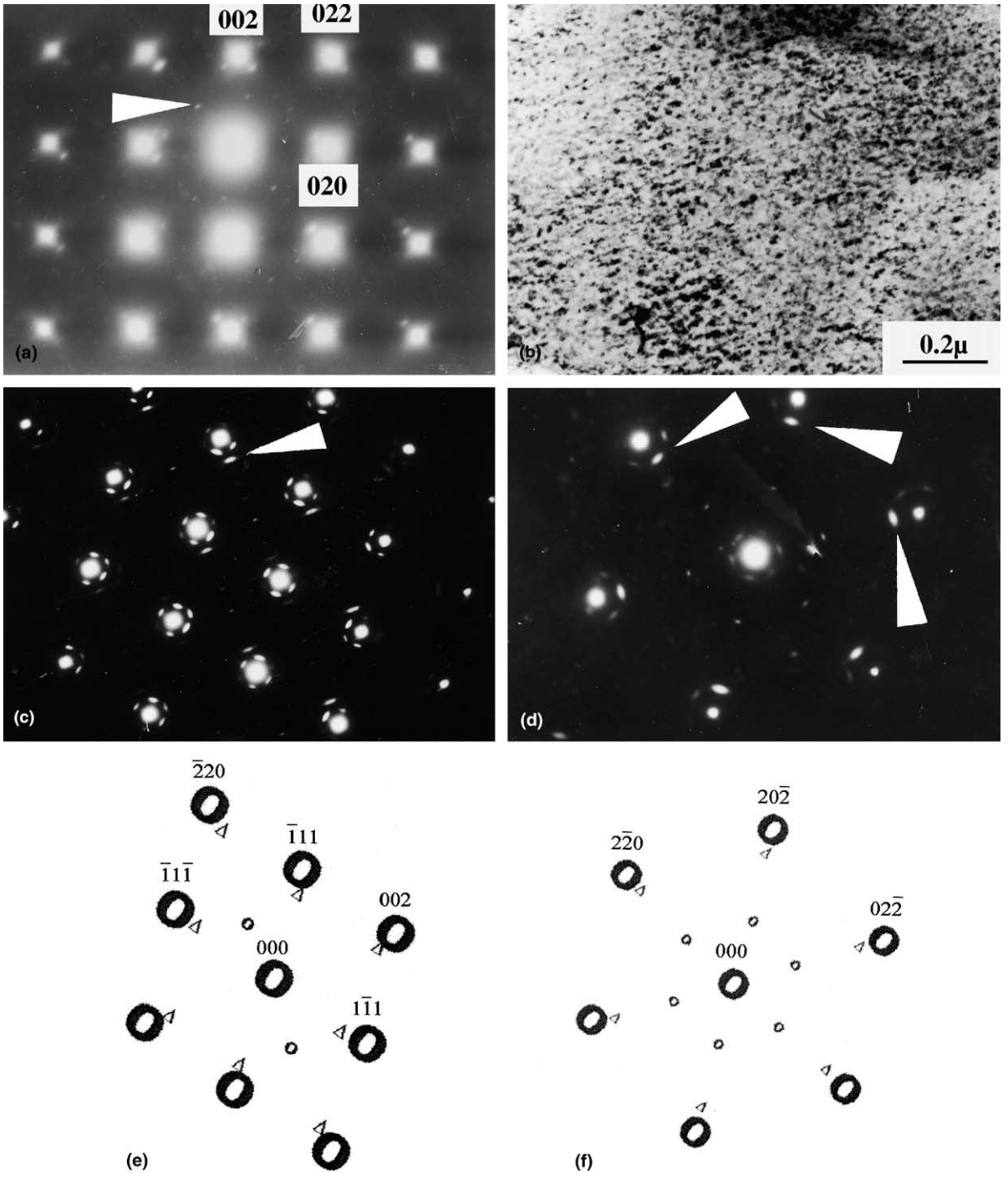

Fig. 7. (a) [1 0 0] SAD pattern from the solutionised plus aged alloy showing streaks along $\langle 1\,1\,0\rangle^*$ around the fcc reflections. These arise due to solute segregation in the initial stages of the decomposition process. The streaks can also be seen to have condensed into reflections of the second phase. A superlattice reflection midway between such a spot and the transmitted spot has been marked by an arrow. (b) BF micrograph showing mottled contrast in the initial stages, (c) [1 1 0] and (d) [1 1 1] SAD patterns showing extra reflections from the ordered fcc precursor having a cube-on-cube OR with the matrix, (e) Key to c, (f) Key to d. Keys e and f show positions of the fundamental (Δ) and superlattice (○) reflections from the precursor and fcc matrix reflections (◎). All the other reflections in c and d arise due to double diffraction.

close-packed direction $\langle 1\,1\,0\rangle_{fcc}$ is parallel to a non-close-packed direction $\langle 0\,0\,1\rangle_{bcc}$. In the Kurdjumov–Sachs (K–S) OR, which is usually observed for well-grown precipitates, both the close-packed planes as well as the close-packed directions in the two lattices are parallel.

Although the occurrence of N–W OR has been well established for the fine bcc precipitates that form in the initial stages, atomistic processes leading to this development have remained largely unresolved. In the case of Cu–Be–Co alloy [31], it was observed that changes in the dimensions of the fcc cell due to ordering of Be atoms play an important role in this. The same mechanism appears to be operative in the present case too.

The BF micrograph in Fig. 7(b) shows a mottled contrast indicating that the precursor is in an incipient stage of evolution. In Figs. 7(c) and (d), $[1\,1\,0]_{fcc}$ and $[1\,1\,1]_{fcc}$ SAD patterns from this region are shown. From these, it is quite apparent that the precursor, having an

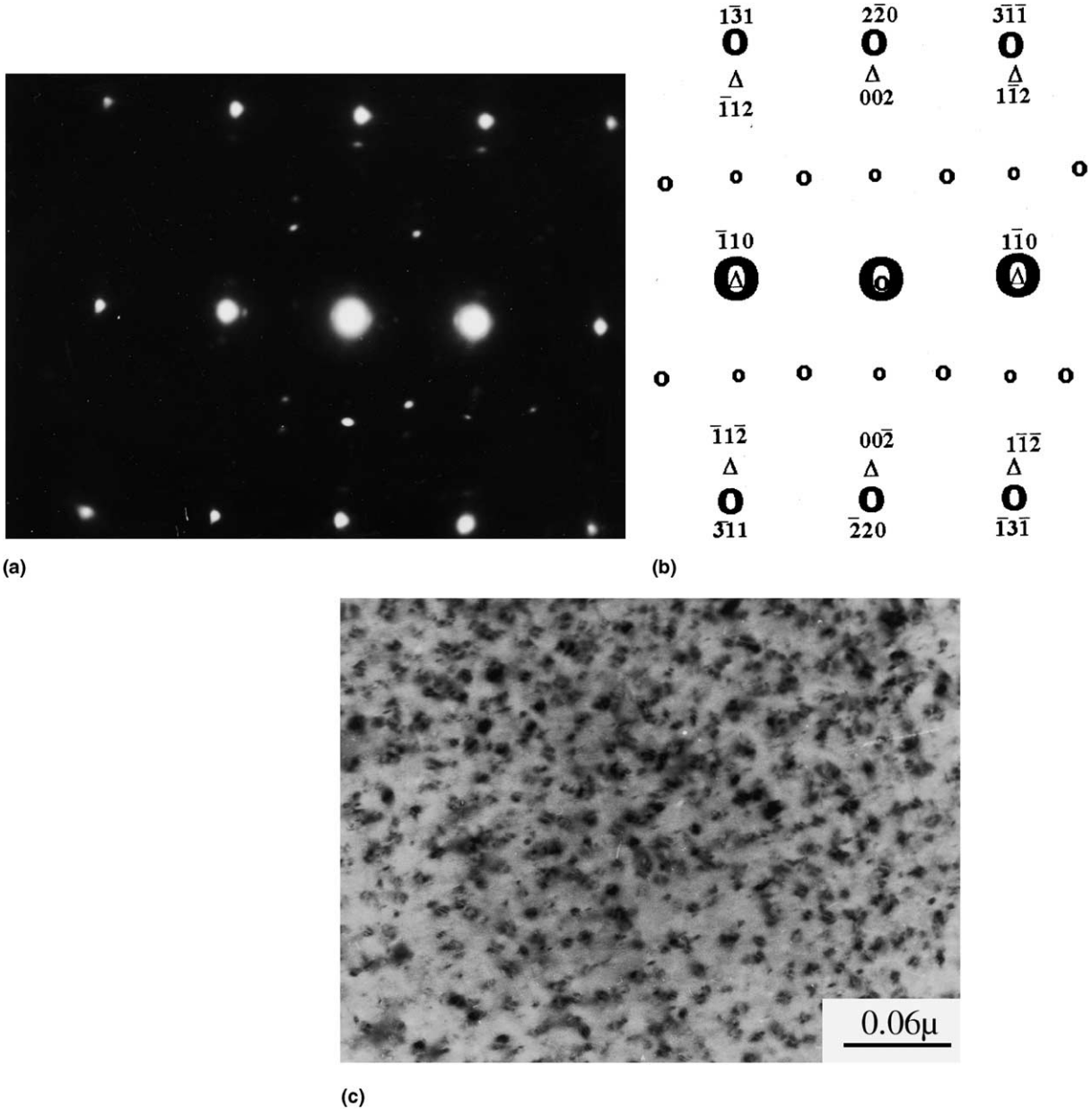

Fig. 8. (a) [1 1 2] SAD from the matrix showing extra reflections from the ordered bcc precipitates. The two phases appear to follow the Nishiyama–Wassermann OR, (b) key to a showing positions of the fundamental (Δ) and superlattice (O) reflections from the bcc precipitates and fcc matrix reflections (O). Distinct precipitates can be seen in the BF micrograph in (c).

ordered fcc structure, exhibits a cube-on-cube OR with the matrix. A curious observation here is that the reflections due to the precursor, having a unit cell larger than that of the matrix, exhibit distinct streaking in certain directions. Consider the row of spots along any one $\langle 220\rangle^*$ from either of these two patterns. It is seen that associated with every $\{220\}$ spot of the matrix is a streaked spot of the precursor (pointed by arrows in Fig. 7(c) and (d)) with a superlattice reflection being midway between the precursor spot and the transmitted spot. Similar rows of spots have also been seen [8,32] in the diffraction patterns of bcc chromium precipitates exhibiting an N–W relationship with the fcc matrix where a $\{200\}_{Cr}$ spot coincides with a $\{220\}$ reflection of the precursor. Other bcc spots expected from the relevant N–W variants are not seen in Fig. 7(c) and (d) and, when seen in totality, the reflections, apart from those of the matrix, can only be indexed as arising from the precursor having a cube-on-cube relationship with the matrix. Ordinarily one would not expect a cube-on-cube OR to give rise to different variants of the product phase. However, with each pair of spots of the precursor streaking in a different direction, a tendency for the formation of variants is quite obvious. Moreover, a good match between d_{200} of bcc chromium with d_{220} of the ordered fcc precursor in the rows of spots along $\langle 220\rangle^*$ suggests that variants of the bcc precipitate, in accordance with N–W OR, are in the process of being formed.

Faint bcc chromium spots forming an entire reciprocal lattice section and exhibiting N–W OR were also observed in some regions of the foil. These are seen clearly in the $[112]_{fcc}$ SAD pattern in Fig. 8(a) and the relevant key in Fig. 8(b). The presence of superlattice reflections at $\{100\}_{bcc}$ and other equivalent positions shows that the precipitates possess a B2 type (CsCl-type) order. A B2 type phase can undergo further ordering to form a $CuMnAl_2$ type ternary ordered structure. The existence of such an ordered phase has been reported by Tang et al. [8] in quaternary Cu–Cr–Zr–Mg. This, however, could not be ascertained in the present case. Fine but distinct precipitates of the ordered bcc phase could be seen in these regions (Fig. 8(c)). This is in contrast to the precursor, which shows only a mottled contrast arising due to the misfit between the precursor and the matrix.

On the basis of the foregoing, it appears that the precursor having an ordered fcc structure is a vital link between the initial stages of decomposition involving segregation of solute atoms, on the one hand, and the formation of the ordered bcc precipitates, on the other.

3.5. HRTEM observations

In the CTEM observations, we have seen that, in the early stages, the decomposition product appears to exist in different states of evolution having different structures, namely, solute segregation, nano-domains of the precursor and fine ordered bcc precipitates. To further resolve the morphological features of these entities, HRTEM was carried out. Fig. 9(a) depicts a HRTEM micrograph exhibiting lattice fringes associated with $(200)_{Cu}$. The fringe spacing measured from the micrograph was seen to be approximately 0.17 nm, which agrees well with d_{200} of Cu (0.1808 nm).

The HRTEM micrograph in Fig. 9(b) shows the decomposition product in its various states of evolution. It is seen that the decomposition product manifests itself in different sizes and contrast features. The relatively smaller entities (labeled A) appear to have a halo around them and a single line of no contrast within them. Some of the others (labeled B) have a lobe–lobe contrast. Relatively larger entities of this type (Fig. 9(a)) exhibit a large number of well-defined alternate bright and dark parallel Moiré fringes. It can be seen that the lines of no contrast as well as the Moiré fringes lie along $\langle 110\rangle_{fcc}$ directions. This underscores our earlier conclusion that

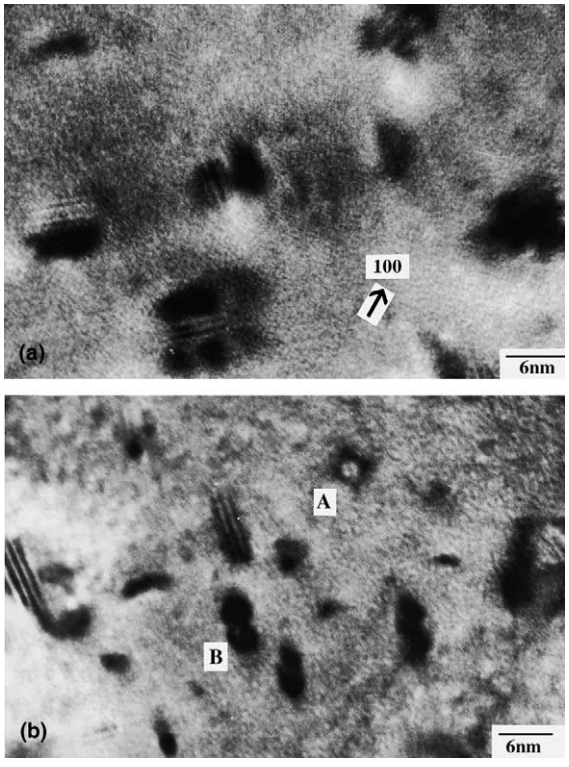

Fig. 9. (a) HRTEM migrograph depicting $(200)_{Cu}$ lattice fringes, particles with lobe–lobe contrast showing Moiré fringes parallel to the lines of no contrast can be seen. The Moiré fringes as well as the lines of no contrast appear to be present in two perpendicular orientations along $\langle 110\rangle$. Particles can be seen to be present in various contrast features in (b) some (A) having a halo around these and some (B) having a lobe–lobe contrast.

the entities seen in Fig. 9 have an ordered *fcc* structure [23]. The Moiré fringes arise due to a small difference in the d-spacings of $\{220\}_{Cu}$ and the associated spot of the decomposition product, shown earlier in the SAD patterns in Fig. 7((a), (c) and (d)). The calculated Moiré fringe spacing (based on the lengths of the relevant *g*-vectors) of 0.825 nm agrees well with the measured value of 0.8 nm. The Moiré fringes being parallel to $\langle 110\rangle_{fcc}$ were found to make an angle of $\sim 45°$ with $(200)_{Cu}$ lattice fringes.

4. Discussion

A sequence of evolutionary stages during the decomposition of the Cu–Cr–Zr alloy is apparent from the results presented in the previous section. The initial decomposition product appears to have an ordered fcc structure with unit cell size larger than that of the matrix. It possesses a cube-on-cube OR with the matrix and appears to be a vital link between the fcc matrix showing just solute segregation, on the one hand, and ordered bcc precipitates, on the other. In this respect, the process of decomposition in this alloy appears to be similar to that in Cu–Be alloy [31] in that, in both the cases, dimensional changes in the fcc lattice brought about by ordering facilitate the formation of the bcc phase. The enlargement of d_{220} of fcc on ordering to d_{200} of the bcc precipitates appears to promote the development of the N–W OR. However, the atomistic processes involved in this step could not be clearly established on the basis of present observations.

Very small additions of zirconium to dilute Cu–Cr alloys are known to have beneficial effects on properties. In commercial purity alloys, dynamic embrittlement is suppressed [33] through the scavenging of sulphur by zirconium. Tang et al. [8] have reported the formation of Cu_4Zr at the grain boundaries during high temperature aging of the high purity quaternary Cu–Cr–Zr–Mg alloy used for divertor applications. In a recent review, Kalinin et al. [34] have commented on the need to control the composition of Cu–Cr–Zr alloys in a narrow range wherein they have pointed out that addition of zirconium in small quantities promotes distribution of precipitates in a more homogeneous manner. Moreover, it influences the peak aging time and the recrystallization temperature.

While we do not contradict the above mentioned roles of zirconium in dilute Cu–Cr alloys, our observations seem to suggest that another important influence of zirconium pertains to the lowering of SFE in these alloys. A lowering of SFE implies [35] a greater propensity for twinning because of a change in the nature of slip from 'wavy' to 'planar'. It is also expected to result in an increased probability of faulting. The observations reported in the present study are consistent with these implications. This readily explains the improved fatigue resistance of the Cu–Cr alloys containing zirconium. Lowering of SFE of copper by zinc or aluminium and that of super austenitic steels by nitrogen was seen to result in improved fatigue behaviour of these alloys through a similar mechanism [27,36]. Yet another important effect of zirconium in dilute Cu–Cr alloys appears to be on the precipitation sequence and kinetics. In contrast to the precipitation sequence in the binary Cu–Cr alloys, addition of zirconium was found to promote the nucleation of an ordered fcc structure from solute-rich clusters, which eventually transformed to ordered bcc precipitates.

Although the properties of the present alloy – thermal, electrical and mechanical – were found to be acceptable for fusion reactor applications, on the basis of the results reported here and other related studies [11], it appears that there is scope for further development of this alloy and design of new alloys.

5. Conclusions

1. Significant gains in tensile properties were found to accrue from small additions of chromium and zirconium.
2. Two kinds of second phase particles were observed: (a) coarse chromium particles formed during solidification and left undissolved during solutionising, (b) chromium rich ordered bcc precipitates resulting from the decomposition of the solid solution.
3. The decomposition sequence arrived at, on the basis of this study, can be summarised as: supersaturated solid solution → solute-rich clusters → metastable fcc ordered phase → ordered bcc precipitates.
4. The reported fatigue property improvements due to zirconium could be ascribed to the lowering of the SFE.

Acknowledgements

The authors are thankful to Mr N.T. Parikh and Mr P.G. Adiga, and to Mr B. Dasmajumdar and his team for their help in alloy preparation and rolling, respectively. The assistance rendered by Mrs P. Agashe in the photographic work and Mrs A.B. Menon in typing the manuscript is also gratefully acknowledged.

References

[1] S.L. Boutard, J. Nucl. Mater 174 (1990) 240.
[2] G.J. Butterworth, C.B.A. Forty, J. Nucl. Mater. 189 (1992) 237.

[3] R.J. Livak, H.M. Frost, T.G. Zocco, J.C. Kennedy, L.N. Hobbs, J. Nucl. Mater. 141–143 (1986) 160.
[4] J. Kalinin, R. Matera, J. Nucl. Mater. 258–263 (1998) 345.
[5] V.V. Rybin, D.L. Smith, J. Nucl. Mater. 191–194 (1992) 30.
[6] S.A. Fabritsiev, S.Z. Zinkle, B.N. Singh, J. Nucl. Mater. 233–237 (1996) 127.
[7] H. Holzwarth, H. Stamm, J. Nucl. Mater. 279 (2000) 31.
[8] N.Y. Tang, D.M.R. Taplin, G.L. Dunlop, Mater. Sci. Technol. 1 (1985) 270.
[9] G. Piatti, D. Boreman, J. Nucl. Mater. 185 (1991) 29.
[10] M. Eldrup, B.N. Singh, J. Nucl. Mater. 250–263 (1998) 1022.
[11] H. Holzwarth, M. Pisoni, R. Scholz, H. Stamm, A. Voolean, J. Nucl. Mater. 279 (2000) 19.
[12] B.N. Singh, D.J. Edwards, M. Eldrup, P. Toft, J. Nucl. Mater. 249 (1997) 1.
[13] A.A.F. Tavassoli, J. Nucl. Mater. 258–263 (1998) 85.
[14] J.W. Davies, G.M. Kalinin, J. Nucl. Mater. 258–263 (1998) 323.
[15] K.D. Leedy, J.F. Stubbins, B.N. Singh, F.A. Garner, J. Nucl. Mater. 233–237 (1996) 547.
[16] V. Belous, G. Kalinin, P. Lorenzetto, S. Velikopolskiy, J. Nucl. Mater. 258–263 (1998) 351.
[17] S.A. Fabritsiev, A.S. Pakrovsky, D.J. Edwards, S.J. Zinkle, J. Nucl. Mater. 258–263 (1998) 1015.
[18] S. Tahtinen, M. Pyykkonen, P. Karjalainen-Roikonen, B.N. Singh, P. Toft, J. Nucl. Mater. 258–263 (1998) 1010.
[19] S.A. Fabritsiev, A.S. Pokrovsky, S.Z. Zinkle, D.J. Edwards, J. Nucl. Mater. 233–237 (1996) 513.
[20] M.J. Walravens, JET, R(85)04, 1985.
[21] V. Barabash, M. Akiba, A. Cardella, I. Mazul, B.C. Odegard Jr., L. Plochl, R. Tivey, G. Vieider, J. Nucl. Mater. 283–287 (2000) 1246.
[22] G.C. Weatherly, P. Humble, D. Borland, Acta Metall. 27 (1979) 1815.
[23] T. Fuji, H. Nakazawa, M. Kato, U. Dahmen, Acta Mater. 48 (2000) 1033.
[24] K.J. Zeng, M. Hamalainen, K. Lilius, Scr. Metall. Mater. 32 (1995) 2000.
[25] P. Villars, A. Prince, H. Okamoto (Eds.), Handbook of Ternary Alloy Phase Diagrams, ASM, Metals Park, OH, 1995, p. 8757.
[26] M. Klesnil, P. Luksu, in: Fatigue of Metallic Materials, Materials Science Monographs, vol. 7, Elsevier, Amsterdam, 1980, p. 62.
[27] Z. Wang, B. Gory, Z.G. Wang, Acta Mater. 47 (1999) 307.
[28] R. Haange, in: Seminar on the Mechanical Engineering Aspects of the JET Fusion Project, Institute of Mechanical Engineers, UK, 1984, pp. 1–5.
[29] L.E. Tanner, Philos. Mag. 14 (1966) 111.
[30] M.G. Hall, H.I. Aaronson, K.R. Kinsma, Surf. Sci. 31 (1972) 257.
[31] E.G. Baburaj, U.D. Kulkarni, E.S.K. Menon, R. Krishnan, Phase Transitions 1 (1979) 171.
[32] J.W. Edington, in: Electron Diffraction in the Electron Microscope, Monographs in Practical Electron Microscopy in Materials Science, Part 2, Philips Technical Library, Macmillan, London, 1975, p. 120.
[33] R.D.K. Misra, V. Satya Prasad, P. Rama Rao, Scr. Mater. 35 (1996) 129.
[34] G. Kalinin, V. Barabash, A. Cardella, J. Dietz, K. Ioki, R. Matera, R.T. Santaro, R. Tivey and the ITER Home Teams, J. Nucl. Mater. 283–287 (2000) 10.
[35] A. Rohtagi, K.S. Vecchio, G.T. Gray III, Acta Mater. 49 (2001) 427.
[36] S. Heino, B. Karlsson, Acta Mater. 49 (2001) 353.